Near-Inertial Internal Wave Field in the Canada Basin from Ice-Tethered Profilers

HAYLEY V. DOSSER AND LUC RAINVILLE

Applied Physics Laboratory, University of Washington, Seattle, Washington

JOHN M. TOOLE

Department of Physical Oceanography, Woods Hole Oceanographic Institution, Woods Hole, Massachusetts

(Manuscript received 21 May 2013, in final form 20 September 2013)

ABSTRACT

Salinity and temperature profiles from drifting ice-tethered profilers in the Beaufort gyre region of the Canada Basin are used to characterize and quantify the regional near-inertial internal wave field over one year. Vertical displacements of potential density surfaces from the surface to 750-m depth are tracked from fall 2006 to fall 2007. Because of the time resolution and irregular sampling of the ice-tethered profilers, near-inertial frequency signals are marginally resolved. Complex demodulation is used to determine variations with a time scale of several days in the amplitude and phase of waves at a specified near-inertial frequency. Characteristics and variability of the wave field over the course of the year are investigated quantitatively and related to changes in surface wind forcing and sea ice cover.

1. Introduction

The Arctic Ocean is undergoing rapid changes. The reduction in summer sea ice cover in recent years (Serreze et al. 2007), coupled with an increase in ocean surface forcing by storms (Hakkinen et al. 2008), may be driving an increase in seasonal internal wave generation (Rainville et al. 2011), though this correlation has not been well quantified. As the Arctic Ocean continues to respond to a changing climate, there is an expectation of increased mixing associated with internal waves over both the shelves and in the deep basins, particularly for wind-generated motions whose frequency is close to the local inertial frequency. As such, the need for multiyear time series of internal wave activity in the Arctic is increasing.

Surface generation of internal waves in the Arctic is primarily a result of surface forcing by wind and the motion of sea ice (D'Asaro 1985), both of which transfer momentum to the ocean surface mixed layer. This forcing results in perturbations at the base of the mixed layer and in the halocline. These density perturbations define an internal wave propagating in both the vertical and horizontal directions. Free internal waves in a resting ocean have frequencies that fall between the local inertial frequency f and the background buoyancy frequency N. Typically, there is a peak in wave energy and shear associated with near-inertial waves at the low-frequency end of the spectrum: frequencies between f and roughly $1.1f$ (Garrett 2001). These near-inertial waves have horizontal wavelengths on the order of kilometers, vertical wavelengths on the order of 10–100 m, and have been observed to dominate the internal wave field in the Arctic (Pinkel 2005).

Previous observations of internal waves in the Arctic have been temporally as well as spatially limited, lacking year-round or multiyear time series. Observations from ice camps, such as the Arctic Internal Waves Experiment (AIWEX; Spring 1985) (Levine et al. 1987; D'Asaro and Morehead 1991; Merrifield and Pinkel 1996) and the Surface Heat Budget of the Arctic Ocean (SHEBA; 1997/98) experiment (Pinkel 2005) have provided information on the propagation characteristics and spectral distribution of Arctic internal waves.

Under ice cover, Arctic internal waves typically have an energy level from one to two orders of magnitude lower than that seen in other oceans (Levine et al. 1985, 1987). The importance of localized topographic mixing and increased heat flux associated with the internal

Corresponding author address: Hayley V. Dosser, Applied Physics Laboratory, University of Washington, 1013 NE 40th Street, Seattle, WA 98105.
E-mail: hdosser@apl.washington.edu

DOI: 10.1175/JPO-D-13-0117.1

wave field has been highlighted by measurements from research vessels during summer cruises, such as those of D'Asaro and Morison (1992), and more recently Rainville and Winsor (2008), Fer et al. (2010), and Lenn et al. (2011). There is also the potential for mixing due to internal waves to modify the unique stratification features found in the Beaufort gyre region, which are described in detail in section 2. Current observational efforts, for example the Ice Covered Ocean Response to Atmospheric Storms (ICORTAS) moorings on the Beaufort shelf (Martini et al. 2013, manuscript submitted to *J. Phys. Oceanogr.*) and the expendable current profilers deployed near the North Pole (Guthrie et al. 2013), aim to provide temporal information about the wave field and its forcing.

The focus of the present work is the quantification of near-inertial internal wave amplitudes from ice-tethered profiler (ITP) observations (Krishfield et al. 2008; Toole et al. 2011) collected in the Canada Basin region of the Arctic Ocean. The ITP instruments are moored in large ice floes and drift with the ice throughout the year. They record vertical CTD profiles with high vertical resolution from near the ice–ocean interface to the base of the Atlantic water layer. ITPs have collected year-round continuous time series since 2004, with data from over 60 instruments publicly available and new instruments deployed each year (http://www.whoi.edu/itp). A significant number of these ITPs collected data in the Beaufort gyre region of the Canada Basin, many as part of the Beaufort Gyre Exploration Project (BGEP) (http://www.whoi.edu/beaufortgyre). Year-round and multiyear ITP measurements with wide spatial coverage can provide a quantitative picture of the seasonality and long-term time evolution of the internal wave field in the Arctic Ocean.

ITPs have been used to study large-scale and mesoscale properties of the Beaufort gyre under sea ice cover, including freshwater content and stratification changes over the past decade (Proshutinsky et al. 2009), seasonal mixed layer evolution (Toole et al. 2010), and the eddy field of the Canada Basin (Timmermans et al. 2008b). An ITP equipped with a velocity sensor has recently been deployed in the Arctic and used to estimate high-frequency motions associated with internal waves (Cole et al. 2013, manuscript submitted to *J. Phys. Oceanogr.*). Most ITPs, however, only measure scalar fields and extracting the near-inertial internal wave field from a typical ITP dataset is nontrivial. The sampling schedule of the ITPs is generally not designed to capture internal waves, but rather to mostly eliminate aliasing due to motions at the semidiurnal tidal frequency and near the inertial (or Coriolis) frequency f, while still sampling infrequently enough to provide measurements over a year or more. The goal of this study is to demonstrate that, despite these limitations, it is possible to accurately quantify near-inertial wave properties using the existing ITP dataset. The instrument and dataset are discussed in section 2, while the technique used to determine vertical displacement amplitudes associated with the near-inertial waves is described in section 3. Uncertainty in the wave amplitude estimates is quantified in section 4, while the resulting near-inertial wave field and connections to atmospheric forcing and sea ice cover are presented in section 5.

2. Data

The ITP data used herein were collected by three instruments (ITP 4, ITP 5, and ITP 6), which drifted in the Beaufort gyre region of the Canada Basin between early September 2006 and early September 2007. The region traversed by these three instruments has relatively simple bathymetry (Fig. 1a). ITPs are anchored in the sea ice by a surface buoy and sample the water column from ~7 m below the surface to 750-m depth. Temperature and conductivity are measured at 1 Hz by a Sea-Bird Electronics CTD, and these data are transmitted by an inductive link to a surface unit, where they are relayed to shore by the Iridium satellite system (Krishfield et al. 2008). The ITP data are mapped to a pressure grid using 1-dbar bin averaging. While the instrument itself remains moored in a perennial ice floe, the surrounding sea ice cover changes seasonally, with thinner, patchier ice in the summer.

Stratification in the central Beaufort gyre is determined primarily by salinity, with several distinct water masses (Fig. 1b). The near-surface mixed layer extends from the surface to between ~10- and ~50-m depth, frequently terminating in a sharp halocline, as discussed by Toole et al. (2010). Below this is the seasonal near-surface temperature maximum (NSTM) (Jackson et al. 2010; Steele et al. 2011), observed above the local temperature maximum caused by the intrusion of Pacific summer water (PSW). A strongly stratified halocline associated with the Atlantic water layer begins at a depth of about 200 m, within which temperature and salinity increase monotonically with depth. In the Beaufort gyre, the Atlantic water temperature maximum is found near 400-m depth.

Above the Atlantic water temperature maximum, double-diffusive processes create a staircase-like stratification profile (Timmermans et al. 2008a). The staircase is composed of multiple density layers in which both temperature and salinity are constant, separated by thin interfaces in which both temperature and salinity increase with depth. Layers can range in thickness from one to tens of meters. Below the double-diffusive staircase are interleaving Atlantic water layers characterized

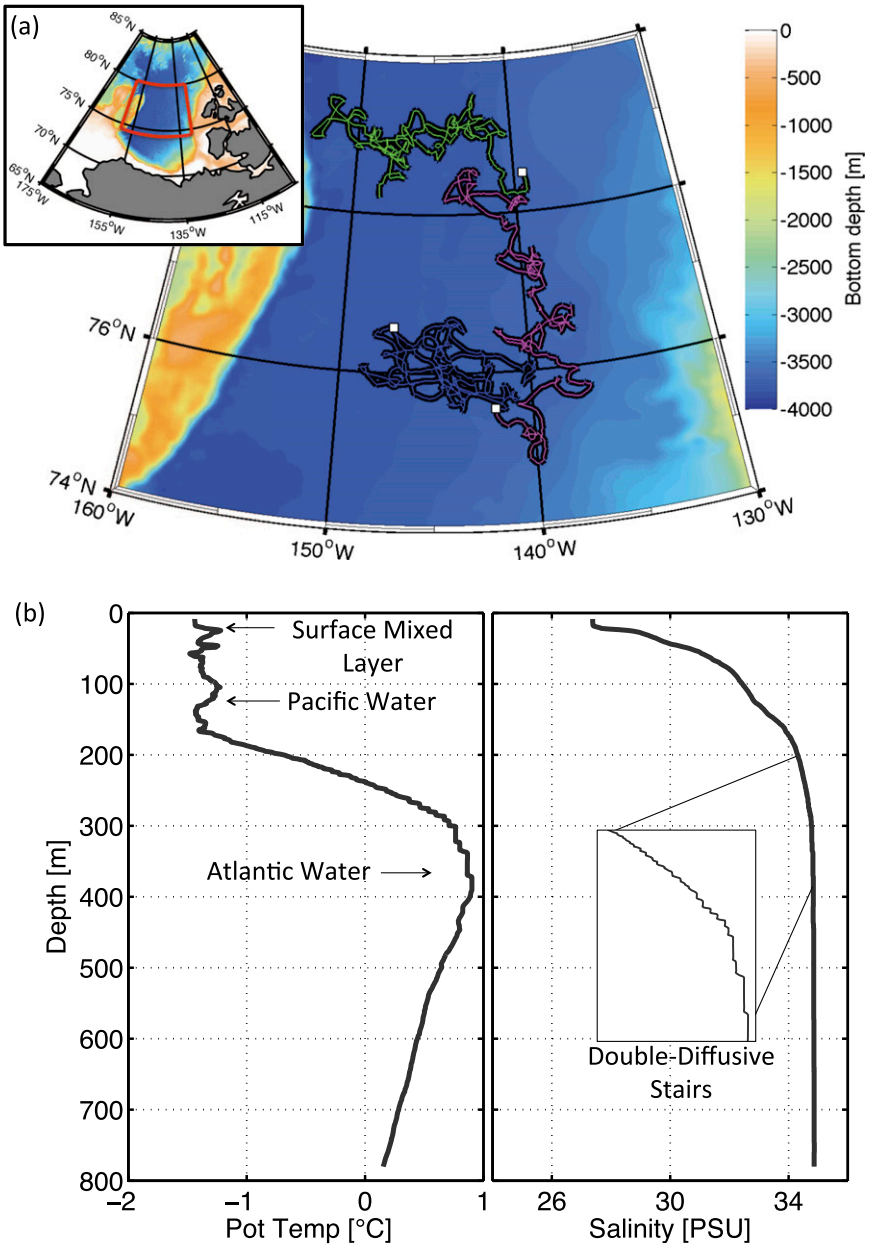

FIG. 1. (a) Trajectories of ITP 4 (green), ITP 5 (blue), and ITP 6 (pink) in the Beaufort gyre region (inset) of the Canada Basin from early September 2006 to early September 2007. White squares mark the end of each record. Color shading shows bathymetry. (b) Typical ITP potential temperature and salinity profiles for the Canada Basin from 6 Sep 2006. The double-diffusive staircase stratification extends from the top of the Atlantic layer to the Atlantic water temperature max.

by thermohaline intrusions (Walsh and Carmack 2003; McLaughlin et al. 2009).

The typical sampling schedule for the ITP instruments is two one-way vertical profiles per day beginning at 0000 and 0600 UTC. The instrument moves vertically along the wire at approximately $\sim 0.25\,\mathrm{m\,s^{-1}}$; profiles to 750 m typically take less than 1 h. The time separation at a given depth between pairs of profiles is thus depth dependent, with samples near the surface separated by less than 6 h and samples at depth by more than 6 h. This uneven sampling schedule was designed so that each pair of profiles is separated by roughly half a semidiurnal tidal/inertial period (which are within 2% of each other in the central Arctic): a near-inertial wave crest measured

at 0000 would be followed by a wave trough at around 0600. Within the Canada Basin, the inertial period varies between $T_f = 12.15$ h at 80°N and $T_f = 12.45$ h at 74°N. The time resolution from the ITP is not sufficient to determine daily variations in the near-inertial wave field, nor to perform an accurate frequency decomposition. This paper demonstrates that it is possible, however, to use ITP data to quantify variations in the amplitude of near-inertial waves over a time scale of a few days.

3. Method

A linear near-inertial wave is associated with a sinusoidal vertical displacement $\eta_I(t) = A_\eta \cos(-\omega t + \phi)$, where ω is wave frequency, and ϕ is phase. This signal is captured, although poorly, by most ITPs deployed to date. To obtain an estimate of the near-inertial wave amplitude $A_\eta(z, t)$, equivalent to half the maximum peak-to-trough vertical displacement, vertical displacements of isopycnals are tracked through time and a complex demodulation is performed on the subdaily displacements. Simply taking the difference between pairs of profiles separated by ~6 h would result in a systematic underestimation of wave amplitudes (by 36% on average).

The total vertical displacements of the isopycnals

$$\eta(z,t)_{\text{tot}} = \eta_{\text{low}} + \eta_{\text{I}} + \eta_{\text{IWS}} + \epsilon \qquad (1)$$

are a combination of low-frequency (subinertial) vertical heaving η_{low}, random noise in the data (uncertainty in isopycnal depth) ϵ, and high-frequency oscillations, which can be expressed as a superposition of near-inertial internal waves η_{I}, and (superinertial) motions associated with the continuum internal wave spectrum η_{IWS}. Plueddemann et al. (1998) noted that near-inertial oscillations dominate on time scales of less than a day. The impact of η_{IWS} and ϵ on the accuracy of the near-inertial displacement estimates is discussed in section 4.

In the Canada Basin, the M_2 and S_2 tidal frequencies fall within the near-inertial band. Barotropic tides in the Beaufort gyre are generally weak (Kowalik and Proshutinsky 1994; Padman and Erofeeva 2004), and are not expected to generated large internal tides, particularly considering the smooth bathymetry of the central Canada Basin. Furthermore, because most of the Canada Basin lies above the critical latitudes for the semidiurnal and diurnal tides, remotely generated internal tides cannot propagate across the basin and do not contribute to the observed isopycnal displacements for the three ITPs discussed here. Topographically trapped internal tides (e.g., Fer et al. 2010) will not be present away from rough topography. Vertical isopycnal displacements are therefore assumed to be primarily associated with wind-driven inertial motions.

a. Isopycnal displacements

Vertical displacements of isopycnals throughout the sampled water column (Fig. 2a) are estimated by tracking potential density (henceforth referred to as density) surfaces corresponding to the initial profile for each ITP, from early September 2006. Potential density is calculated relative to the surface from the base of the mixed layer to the base of the double-diffusive staircase at 400 m and calculated relative to 400 m for the remainder to the water column. This deeper reference level ensures that the derived potential density profile for lateral density intrusions below the Atlantic water temperature maximum increases monotonically with depth. The choice of 400 m does not impact the resulting vertical displacement estimates.

Tracked isopycnals were initially separated by 1 m in the vertical, with the exception of the double-diffusive staircase in which individual density steps were tracked instead. No value is recorded if an isopycnal is statically unstable at a given time. Isopycnal depths can be determined for over 90% of all data points over the course of the year.

Within the double-diffusive staircase, vertical displacements are estimated by tracking the depth of the top and bottom of each constant density step, for which the second derivative of potential temperature with depth is at a minimum or a maximum, respectively. This secondary condition on potential temperature is used in addition to density to avoid issues with conductivity sensor lag at sharp density interfaces (Johnson et al. 2007). This procedure is also used for the interleaving Atlantic water layers immediately below the staircase.

Following the idea that the average of two profiles taken exactly half an inertial period apart would exclude the inertial signal, low-frequency heaving with periods of a day and more is removed (Fig. 2b) by subtracting the average of each pair of profiles

$$\eta = \eta_{\text{tot}} - \eta_{\text{low}} = \eta_{\text{tot}} - \frac{1}{2}(\eta_{0:00} + \eta_{6:00}). \qquad (2)$$

This is similar to how Leaman and Sanford (1975) separate the inertial signal from low-frequency motions. This decomposition is not perfect, particularly because of the finite time the instrument requires to profile and because the inertial period is not exactly 12 h. Presumably a small amount of noninertial high-frequency variance (i.e., η_{IWS}) is also mapped into η_{low} and removed. However, this decomposition takes advantage

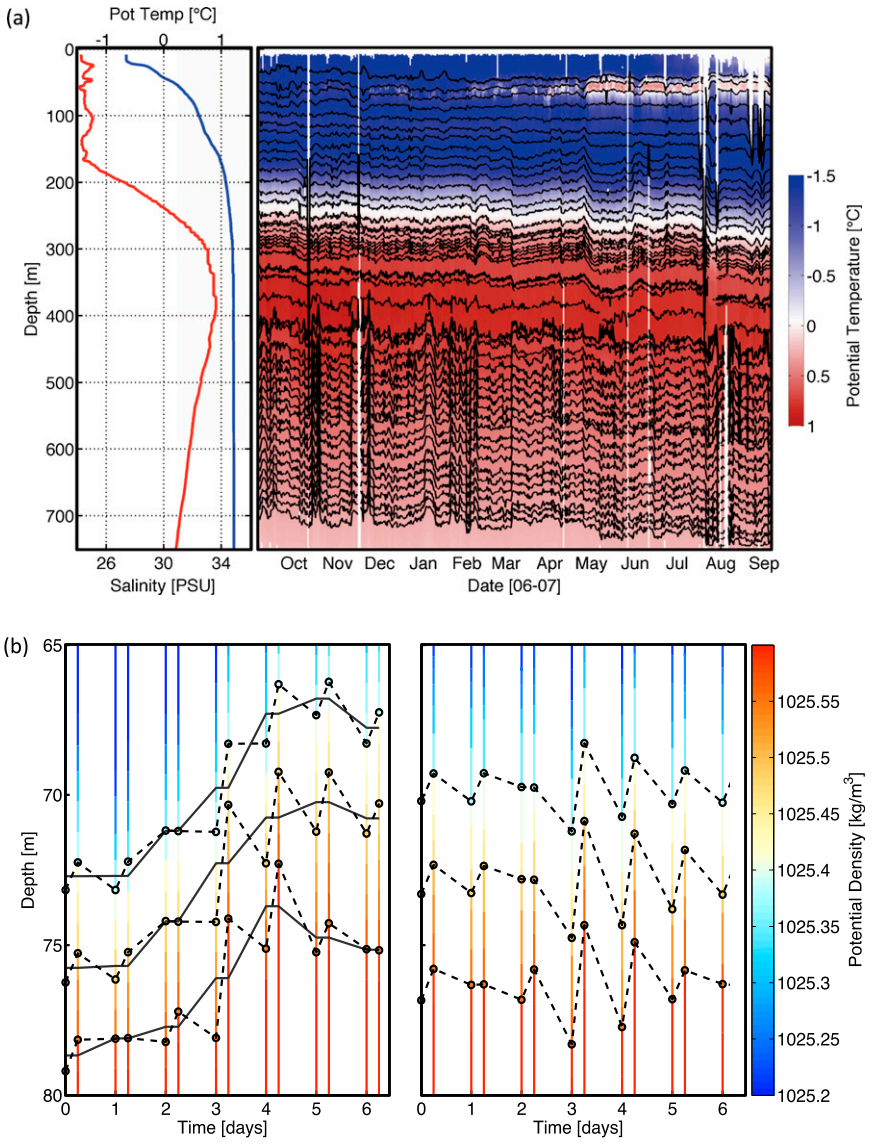

FIG. 2. (a) Potential temperature (red) and salinity (blue) profiles as in Fig. 1b (left) and depths for a subset of isopycnals (black lines–plotted roughly every 15 m) for ITP 6 (right). The colors indicate potential temperature. (b) Three sample isopycnals over a 7-day period. The colored vertical lines are potential density values, the dashed black lines show the depths of the isopycnals, and the thick gray line shows the mean vertical displacement calculated as a "daily average" (left). The same three isopycnals with the mean removed, leaving only displacements near the inertial frequency (right).

of the sampling of the ITP and provides a consistent definition of the low-frequency field with minimal aliasing of the inertial displacements.

b. *Complex demodulation*

Slow time variations in A and ϕ for periodic motions at ω are estimated using complex demodulation (Emery and Richard 1998). Least squares harmonic fits are applied to overlapping segments of isopycnal displacements $\eta(t)$ [Eq. (2)], using a cosine wave of the form $A_\eta \cos(-\omega t + \phi)$. Near-inertial waves are assumed to be coherent for at least ~8 wave periods, so that a 4-day window of data can be used for each cosine fit. This technique can be used with unevenly spaced data, and requires only that the segment of data be longer than one wave period, and that the number of points be much higher than the number of frequencies to fit.

The near-inertial frequency used is $\omega = 1.05f$, (where f varies with latitude as the ITP drifts). It was determined that $\omega = 1.05f$ explained the most variance in the data

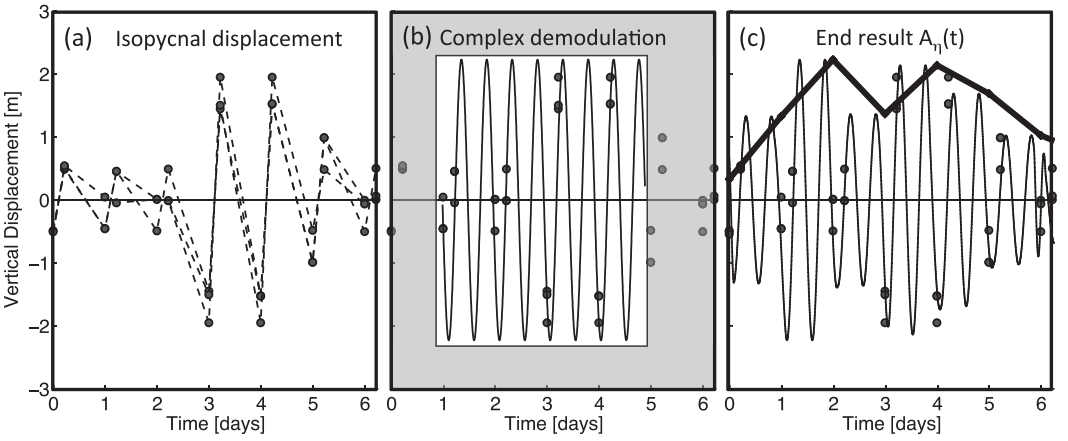

FIG. 3. (a) Data: Vertical displacements for an isopycnal from Fig. 2b combined with the isopycnals immediately above and below to give 24 data points (gray dots) per 4-day window. (b) Method: A harmonic least squares fit ($\omega = 1.05f$) to each window of data gives the amplitude and phase of the ideal cosine (thin black line) that best explains the variance in the data. (c) Result: The complex demodulation procedure produces a slowly varying $A_\eta(t)$ (thick black line) and $\phi(t)$ (not shown) corresponding to a near-inertial wave (thin black line, extrapolated using linear interpolation between daily values for A_η and ϕ).

overall. The amplitude estimates were, however, relatively insensitive to the particular choice of near-inertial frequency ω, in the range from $0.9f$ to $1.1f$.

Vertical displacements for each isopycnal are combined with those of the isopycnals immediately above and below, tripling the number of data points per fit and reducing the impact of random noise. This assumes wave coherence over ~2–5 m in the vertical. For each time window, the amplitude and phase of the near-inertial wave that best explains the data are obtained (Fig. 3). The window is then shifted forward in time by one day, and a new amplitude and phase estimate are determined.

Waves with a frequency very different than the fitted frequency, or waves that are coherent for less than roughly 4 days, are not well captured using this technique. Cosine fits that explain little variance in the data are excluded based on the coefficient of determination R^2 value, which is calculated from

$$R^2 = 1 - \frac{\sum(\eta_{\text{data}} - \eta_{\text{fit}})^2}{\sum(\eta_{\text{data}} - \overline{\eta_{\text{data}}})^2}, \tag{3}$$

where, for each segment of time, η_{data} gives measured vertical displacements, η_{fit} gives vertical displacements of the ideal cosine wave, the overbar denotes the time average of η_{data}, and the sum is taken over the 24 points in a given 4-day window (2 profiles per day, over 4 days, for 3 isopycnals). Any fit with an R^2 value of ≤ 0.25 (explaining 25% or less of the variance in the data) is excluded from the results. The A_η of any fit is also restricted to be less than 1.5 times the maximum measured displacement over the 4-day window.

The average R^2 value for the entire wave field for ITP 6 is $R^2 = 0.6$; in other words, 60% of the variance in the observed near-inertial vertical displacements can be explained by slowly varying near-inertial waves (Fig. 4). Values are comparable for ITPs 4 and 5.

4. Uncertainty analysis

Several factors contribute to the uncertainty of the near-inertial wave field estimated using the method outlined in the previous section. This section investigates uncertainty caused by errors in the determination of isopycnal depths, by the presence of motions at super-inertial frequencies (internal wave continuum), and by the range of near-inertial frequencies present in the wave field (relative to the specified frequency of $1.05f$).

The determination of isopycnal depths is limited by instrument noise. It is also limited by the vertical spacing between the processed salinity and temperature data provided by the ITP group (1 dbar). Because dissipation is so small in the Arctic Ocean, observed density inversions are likely instrument noise as opposed to actual overturns (Johnson and Garrett 2004). The Thorpe displacements (Thorpe 1977) are thus used as a measure of uncertainty in isopycnal depth [ϵ in Eq. (1)].

Above the thermohaline staircase, the depth of an isopycnal is known to within 1 m, while for the water column below it is known to within 2 m. These values are comparable to the vertical spacing of the data points. Within the double-diffusive staircase, it is difficult to determine the noise ϵ; however, it is expected to be of the same order as in the water column above. The possibility

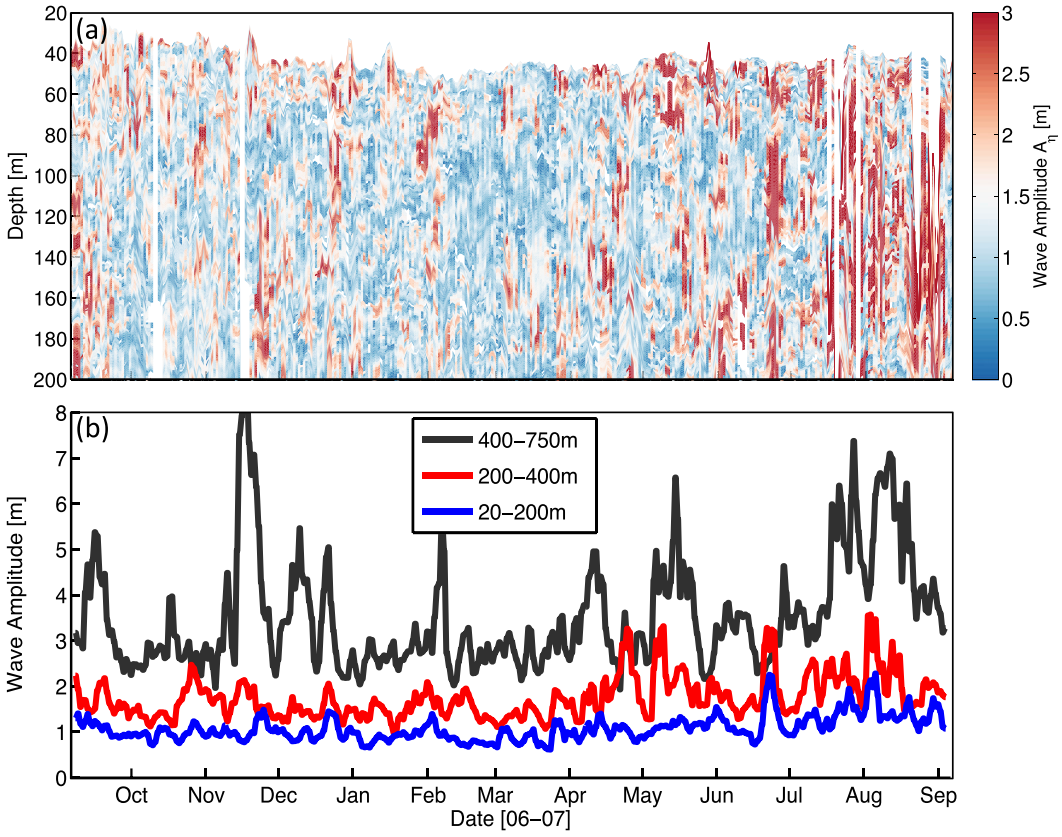

FIG. 4. (a) Vertical displacement wave amplitude field for one full year of data from ITP 6, over the top 200 m of the water column. Waves with larger vertical displacements are red. Gaps are regions without data, or for which $R^2 < 0.25$. (b) Depth-averaged vertical displacement wave amplitude for the top 200 m (blue line), the double-diffusive staircase region from 200 to 400 m (red line), and the lower water column from 400 to 750 m (gray line).

of a small systematic bias between the up- and downward ITP profiles used to determine isopycnal depth was investigated but was found to contribute negligibly to the overall error in the wave field.

To account for potential aliasing of high-frequency internal waves into the near-inertial wave estimates, isopycnal displacements consistent with the spectral shape of the Garrett–Munk (GM) model of internal waves (Garrett and Munk 1972; Gregg and Kunze 1991), but an order of magnitude smaller (Levine et al. 1985; the appendix), are included in the uncertainty analysis.

Statistical estimates of uncertainty in the near-inertial wave amplitudes are obtained using Monte Carlo simulations. The complex demodulation method is applied to an ensemble of 300 known test waves with arbitrary phase and a specified (near inertial) frequency of $1.05f$. Each test wave is subsampled to match the ITP sampling as outlined in the previous section. The uncertainty δA_η is taken to be two standard deviations (95% confidence interval) from the mean difference between the amplitude estimates and the known test wave amplitude. This procedure is repeated for every latitude and sampling interval considered in the analysis of the ITP data.

Variance in the data not associated with near-inertial waves is accounted for by adding random noise consistent with the uncertainty in isopycnal depth ϵ and variance consistent with the continuum internal wave spectrum $\eta_{\mathrm{IWS}} = \mathrm{GM}/10$ onto a known test wave. This causes an absolute error in wave amplitude of ± 0.5 m above the double-diffusive staircase, ± 1.0 m within the staircase, and ± 1.5 m below. The variation with depth is a result of the increase in ϵ and the decrease in stratification with depth. In the absence of a near-inertial wave, the complex demodulation method is unable to find an appropriate cosine fit to $\epsilon + \eta_{\mathrm{IWS}}$ over 90% of the time, as expected. When subsampled to match the ITP, a time series consistent with GM/10 appears similar to random noise (Fig. 5) resulting in wave amplitude estimates that are statistically indistinguishable from zero.

Varying the frequency of the known test wave between f and $1.1f$ (relative to the specified cosine fit frequency of $1.05f$) causes a relative (percent) uncertainty

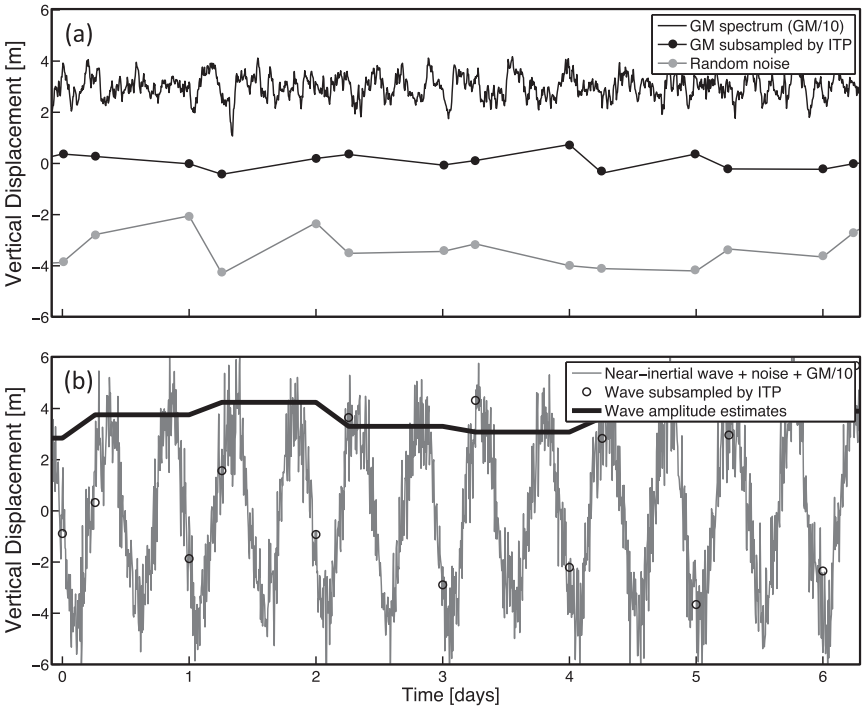

FIG. 5. (a) Time series consistent with variance at the GM/10 spectral level (black line, vertically offset by 3 m), subsampled to match the ITP (black dotted line), appears similar to random noise (gray dotted line, vertically offset by −3 m). (b) Time series for a known near-inertial test wave with an amplitude of 4 m with GM/10 and random noise superimposed (gray line). This wave is subsampled to match the ITP (black circles), and wave amplitudes estimates are determined using complex demodulation (thick black line).

in the wave amplitude of between $25\%A_\eta$ and $40\%A_\eta$ (Fig. 6a). This relative uncertainty varies slightly with depth because of the changing sampling interval between pairs of data points but is predominantly affected by the latitudinal dependence of the local inertial frequency. Uncertainties are higher when the time interval between measurements is almost equal to half the local inertial period. The restrictions on the R^2 value for a given fit and on the maximum amplitude relative to the measured displacements ensure that fits that are badly constrained are excluded from the wave amplitude estimates. A typical relative uncertainty is $\sim 30\%A_\eta$.

The uncertainty reported in section 5 includes both the absolute and relative uncertainty. This uncertainty is ±2 m or less for most amplitude estimates. The average is ±1 m, with 95% of amplitudes inferred from the dataset accurate to within ±3 m or better (±1 m for the top 200 m). The large majority of wave amplitude estimates (section 5) are thus statistically significant and are a good representation of the variance in the data points regardless of associated uncertainty (Fig. 6).

Uncertainties from the Monte Carlo simulations do not represent a measure of disagreement between the amplitude estimates and the variance in the data points, which is quantified by the coefficient of determination R^2 (section 3). Rather, they characterize how accurately the ITP measurements are able to capture the wave field in the presence of numerous sources of uncertainty.

5. Discussion

The goal of this work is to quantify the near-inertial wave field from ITP data. The vertical displacement amplitude for near-inertial waves, and its associated uncertainty, is estimated for three ITPs that sampled in the central Canada Basin during 2006/07. This field, shown in Fig. 4a for the top 200 m of the water column sampled by ITP 6, can be connected to physical processes influencing the waves, such as sea ice cover and wind forcing.

During winter, wind speeds are typically higher, and fractional sea ice cover is typically nearly 100% in the Beaufort gyre region. During summer, the fractional sea ice cover and ice thickness in the area around the ITP can decrease significantly. The instrument itself remains moored in a large ice floe ideally composed of thick

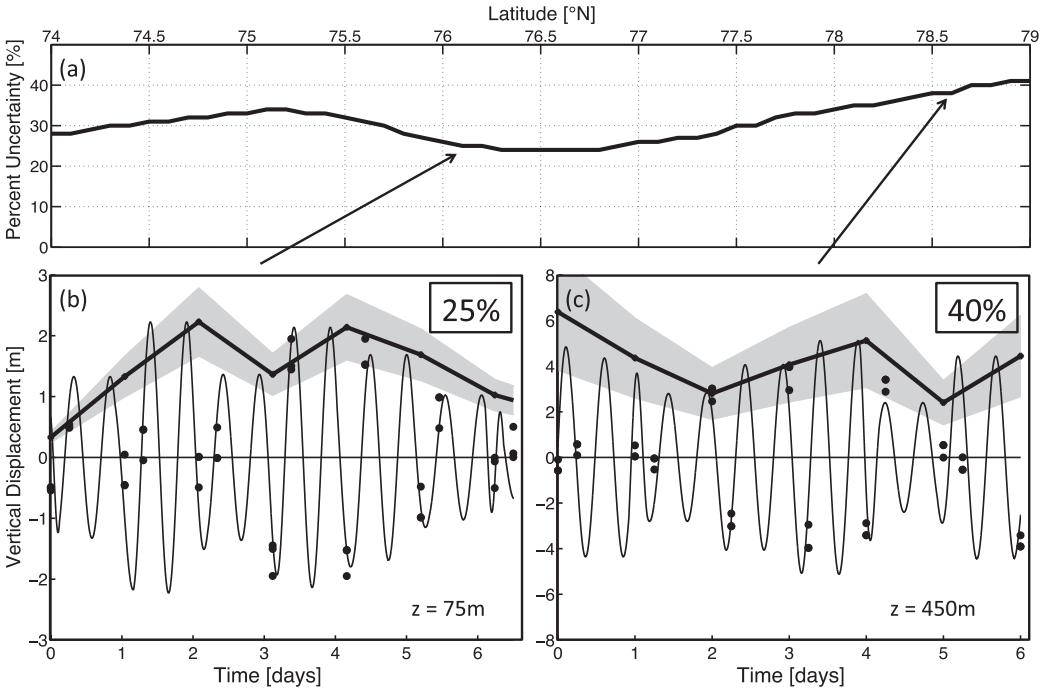

FIG. 6. (a) Uncertainty (%) in the wave amplitude estimates as a function of lat based on Monte Carlo simulations. (b) Example of 25% uncertainty in amplitude. Black dots are near-inertial vertical displacements from ITP 6 measured near the surface over 7 days. The thin black line shows the cosine wave fits determined using complex demodulation. The thick black line gives the associated vertical displacement amplitude estimates. The gray band shows the uncertainty in these estimates through time. (c) As in (b), but for an uncertainty of 40%.

multiyear ice. Wind speeds in summer are typically lower. The ITP drifts with the ice, whose motion is primarily a result of surface wind stress. This results in a strong inertial component to the ice motion, particularly for thinner, patchier summer sea ice, as investigated by Gimbert et al. (2012). The near-inertial wave field will therefore be impacted by both wind forcing and sea ice cover, on a range of time scales.

The amplitudes of the near-inertial waves observed increase with depth as shown in Fig. 4b, reaching 3–5 m on average below 400 m (Fig. 7a), although highly variable, often as large as 10 m or more. When the effects of decreasing stratification are taken into account via Wentzel–Kramers–Brillouin (WKB) normalization (e.g., Pedlosky 2003), most of the large-scale vertical variations in wave amplitude are eliminated (Fig. 7b). The WKB normalization $A_\eta\sqrt{[N(z)/N_0]}$, in which N_0 is the average buoyancy frequency, assumes that the background buoyancy profile $N(z)$ varies slowly and smoothly on a vertical scale much larger than that of the waves.

Depth-averaged WKB-scaled near-inertial wave amplitudes are spatially distributed fairly evenly over all latitudes and longitudes traversed by the ITPs. Topographically generated waves are unlikely due to the smooth bathymetry in the central Canada Basin. The WKB-scaled amplitude varies temporally on time scales from days to many months. On a seasonal time scale, wave energy is lower during winter and increases significantly during summer (Fig. 8a). These variations may reflect seasonal changes in sea ice cover (Fig. 8b). Fractional sea ice cover around the ice floe drifting with each ITP was derived from Special Sensor Microwave Imager (SSM/I) ice concentration satellite data (Cavalieri et al. 2008), gridded in 25-km × 25-km boxes. The mean was removed from each wave amplitude time series and both fields were smoothed using a 30-day low-pass filter. The average percent uncertainty in the depth-averaged WKB-scaled wave amplitude is ~30%, resulting in an overall uncertainty of ±1 m.

As sea ice around the ITPs decreases during summer (July–September), a corresponding increase in wave energy is observed, with an increase in the average wave amplitude of 0.45 m relative to winter (January–March). This change in amplitude represents ~20% of the total variance in the wave field over the course of the year. In the Beaufort gyre region of the Canada Basin, winds and storms are weaker during summer and increase during winter (Overland 2009). In other words, near-inertial wave energy is observed to be highest during summer when winds are weakest, but sea ice cover is reduced.

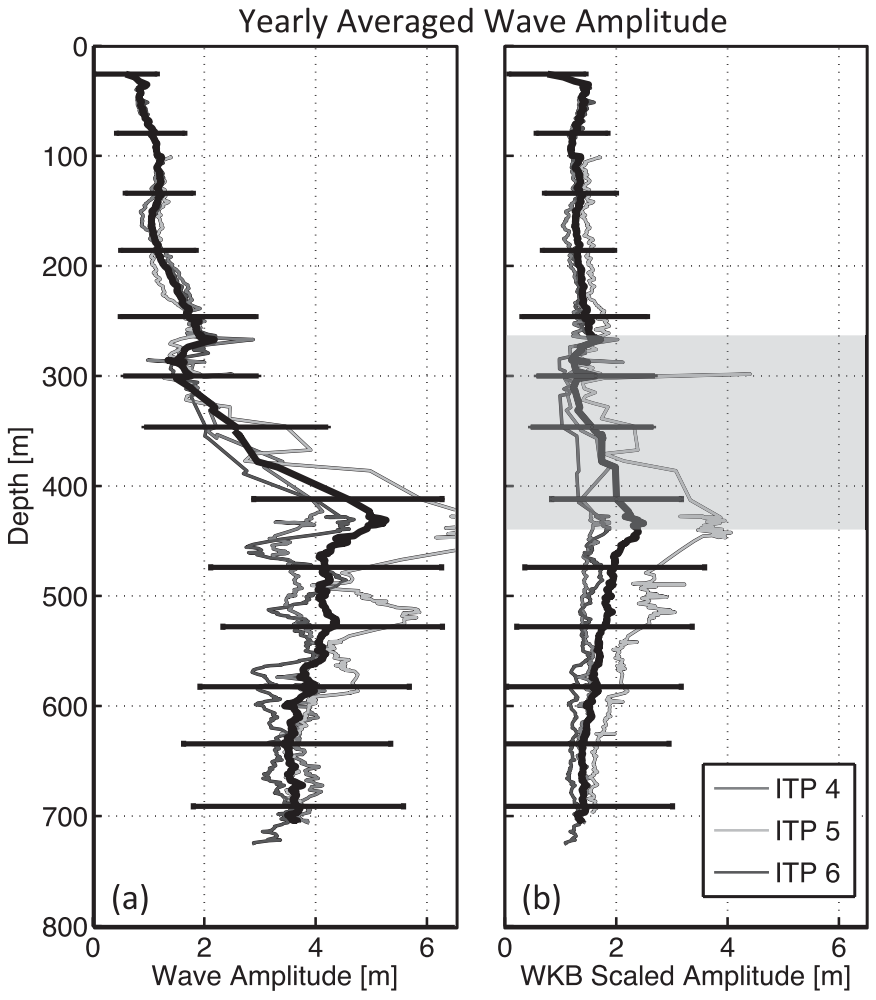

FIG. 7. (a) Time-averaged vertical displacement amplitude A_η vs average isopycnal depth for ITP 4, ITP 5, and ITP 6. The thick black line is the average of the three. The black horizontal lines show the combined error range. (b) As in (a), but for the WKB-scaled time-averaged vertical displacement amplitude $A_\eta\sqrt{[N(z)/N_0]}$. The gray panel indicates depths within the double-diffusive staircase for which WKB normalization is not truly applicable due to sharp changes in $N(z)$.

On a daily time scale, wave energy is higher and more variable during periods of less than 100% sea ice cover (Fig. 9). Increases in wave amplitude tend to be episodic, with sudden jumps in energy associated with sudden decreases in ice fraction around the ITP. During periods of 100% ice cover, wave energy is lower and less variable. The WKB-scaled vertical displacement amplitude from ITP 6 (shown depth-averaged over the top 200 m in Fig. 9), has an overall uncertainty of ± 1 m.

High wind events were frequently associated with peaks in near-inertial wave amplitude (Fig. 10). During winter, sea ice cover inhibits direct wind forcing of the ocean surface and damps near-inertial waves, which may help explain the mismatch between the strength of the wind forcing and the strength of the wave response. Wind stress was determined using National Centers for Environmental Prediction (NCEP)–National Center for Atmospheric Research (NCAR) 10-m winds from the NCEP reanalysis project (Kalnay et al. 1996; Kanamitsu et al. 2002), interpolated from the global grid to the drifting ITP position. At high latitudes, this reanalysis wind data lacks the resolution to resolve the spatial and temporal patterns most efficient at generating near-inertial waves (Alford 2003; Martini et al. 2013, manuscript submitted to *J. Phys. Oceanogr.*).

Despite these limitations, wave amplitude is observed to covary with surface wind forcing (Fig. 10). The depth-averaged WKB-scaled wave amplitude over the top 200 m is weakly correlated with the magnitude of surface wind stress from daily NCEP–NCAR data, following the

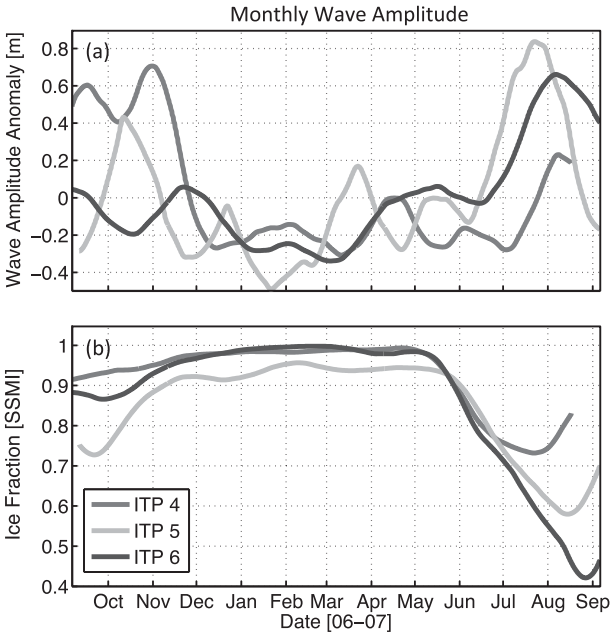

FIG. 8. (a) WKB-scaled depth-averaged vertical displacement wave amplitude $A_\eta\sqrt{[N(z)/N_0]}$ plotted vs time. The mean has been subtracted for each ITP and a 30-day low-pass filter has been applied. The value of the mean is 1.4 m for ITP 4, 2.2 m for ITP 5, and 1.4 m for ITP 6. (b) Fractional sea ice cover around the ITPs over the course of the year, derived from SSM/I ice concentration satellite data and smoothed using a 30-day low-pass filter.

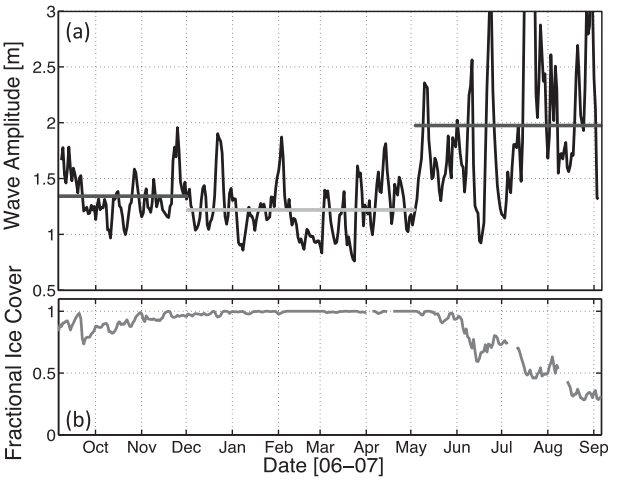

FIG. 9. (a) Daily WKB-scaled vertical displacement wave amplitude $A_\eta\sqrt{[N(z)/N_0]}$ from ITP 6, depth-averaged over the top 200 m. The dark and light gray lines show the mean wave amplitude during periods of <100% sea ice cover and 100% sea ice cover, respectively. (b) The fractional sea ice cover around the ITP over the course of the year, derived from daily SSM/I ice concentration satellite data.

track of ITP 6 (correlation is $R = 0.3$, statistically significant at the 95% confidence level). Both fields have been bandpass filtered between 1/30 and 1/7 cycles per day (cpd) to partially account for the mismatch in seasonal variability.

If only summer months (July–September) are considered, the correlation value rises to $R = 0.5$, significant at the 95% confidence level. For only winter months (January–March), the correlation is $R = 0.3$. If a slight lag of 1–2 days is used during winter, presumably reflecting the time needed for the wind to transfer momentum through the sea ice to the water below, the correlation rises to $R = 0.4$.

The relationship between wind, sea ice, and near-inertial waves is complex, and much remains to be done before a comprehensive understanding of internal wave generation and propagation is reached for the Canada Basin. In the present work, the near-inertial wave field has been quantified using the ITP dataset and shown to have clear connections to physical processes on multiple time scales.

6. Summary

The near-inertial internal wave field in the central Canada Basin from September 2006 to September 2007 is estimated using three ice-tethered profiler instruments. This paper demonstrates that it is possible to use the ITP dataset to extract and quantify the near-inertial wave field at all depths, including regions of complex stratification such as the double-diffusive staircase found in the Canada Basin. The results are accurate, physically reasonable, and the magnitude of the near-inertial wave field can be linked to sea ice cover and surface wind forcing.

On time scales from days to weeks, fluctuations in wave energy are connected to both increased surface wind forcing and decreased sea ice cover, with a weak correlation between wind stress and wave amplitude. On a seasonal time scale, decreased sea ice around the ITP during summer is linked to increased wave energy. Thick winter ice may prevent momentum transfer from winter storms to the ocean, damping wave motion and resulting in a mismatch between wind forcing and the wave response. During summer, thin, patchy ice may allow more direct wind forcing of the surface ocean and increased near-inertial wave generation. There is a quantifiable connection between seasonal changes in sea ice and wave energy for the Canada Basin during 2006/07, with ~20% of the total variance in the depth-averaged wave field explained by changes in sea ice cover.

As seasonal sea ice cover continues to decrease, and the Canada Basin becomes ice free during the summer, it is expected that direct wind forcing on the ocean's surface will significantly alter the properties of the internal wave field, particularly in the near-inertial band.

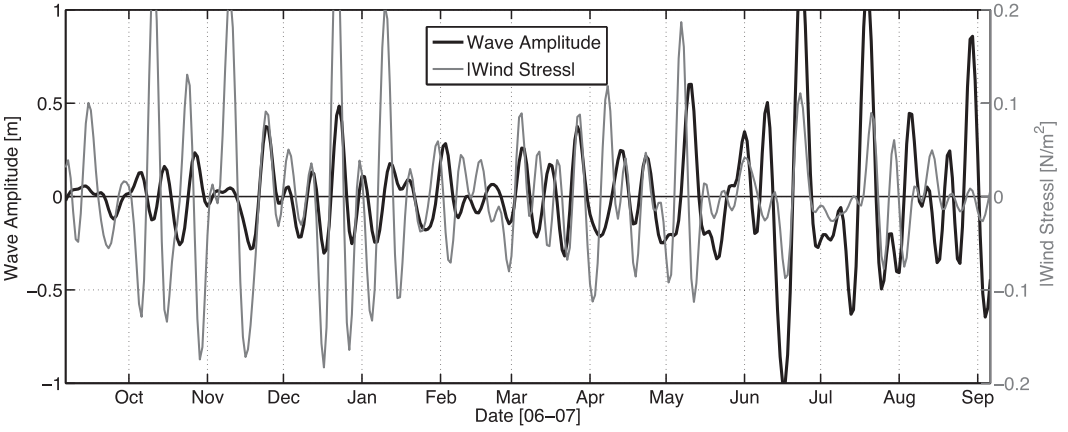

FIG. 10. Time series of WKB-scaled vertical displacement amplitude for ITP 6 (black line), depth-averaged over the top 200 m, and the magnitude of the daily wind stress following the track of ITP 6 (thin gray line). Both fields have been bandpass filtered between 1/30 and 1/7 cpd.

The potential impacts of an evolving internal wave field are significant and include increased vertical heat flux due to wave breaking and an increase in the associated mixing, as well as potential erosion of stratification features such as the double-diffusive staircase and the summer halocline. The extent and magnitude of such changes in the annual and interannual variability of the wave field are currently unknown.

Building on the work presented here, it is possible to investigate and quantify such changes using the greater ITP dataset. The full ITP dataset is extensive, with wide spatial coverage and over 8 years of observations. There are currently several ITPs deployed in the Canada Basin, with more deployments likely during the next several years. Despite their limitations, ITPs provide the best opportunity to investigate the relative roles of wind forcing, sea ice cover, and stratification on the near-inertial wave field in the Arctic Ocean, providing insight into the impact of rapid climate change.

Acknowledgments. We gratefully acknowledge the Ice-Tethered Profiler Program and the Beaufort Gyre Exploration Program based at the Woods Hole Oceanographic Institution (in collaboration with researchers from Fisheries and Oceans Canada at the Institute of Ocean Sciences) for deploying and maintaining the ITPs and the BGEP moorings, as well as processing the data and making it available to the scientific community (http://www.whoi.edu/itp; http://www.whoi.edu/beaufortgyre). The ITP program and J. Toole's contributions were supported by the National Science Foundation Office of Polar Programs Arctic Observing Network. We acknowledge the support of the Office of Naval Research (Grant N00014-11-1-0454) for this study. Support for H. Dosser was also provided by the Natural Sciences and Engineering Research Council of Canada. NCEP Reanalysis Derived data was provided by NOAA/OAR/ESRL PSD, Boulder, Colorado, from their website (http://www.esrl.noaa.gov/psd/). Sea ice concentrations from *Nimbus-7* Scanning Multichannel Microwave Radiometer (SMMR) and Defense Meteorological Satellite Program (DMSP) SSM/I-SSMIS passive microwave data were provided by the National Snow and Ice Data Center, Boulder, Colorado.

APPENDIX

Arctic Internal Wave Spectrum

This section presents observations from a mooring deployed in the central Canada Basin, which confirm that the internal wave continuum in the Arctic is at least one order of magnitude less energetic than at lower latitudes. As part of the BGEP (see Proshutinsky et al. 2009), a bottom-anchored mooring has been deployed near 74°N, 140°W (site D) since 2002. In addition to a moored profiler sampling the properties of the water column between 50 and 2000 m on a time scale of a day, BGEP mooring D was equipped in 2007/08 with an upward-looking Acoustic Doppler Current Profiler (ADCP) mounted on the 50-m subsurface buoyancy sphere, and with fixed-depth temperature sensors in the deep bottom thermohaline staircase (Timmermans et al. 2010). These instruments sampled rapidly and accurately, providing velocity estimates every hour for the ADCP and temperature every 3 min at depth.

While the ADCP does not provide estimates of isopycnal displacements, it allows us to estimate the

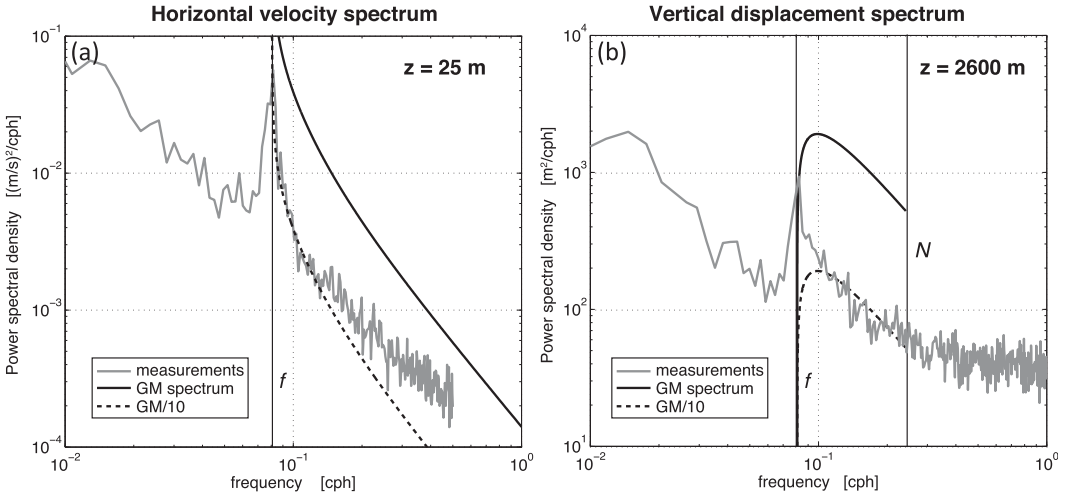

FIG. A1. (a) Horizontal velocity spectrum at 25 m, and (b) vertical displacement spectrum near 2600 m, measured from a mooring deployed near 74°N, 140°W in 2007/08. In both cases, the measured spectra (gray) are about 10 times less energetic than the GM spectral model (black lines).

near-surface horizontal velocity spectrum (Fig. A1a). The annual-mean amplitude of the inertial currents, rotating clockwise in time, at this location is 1.5 cm s^{-1}, with maximum values reaching 6 cm s^{-1} (not shown). These measured inertial currents are of the same order as those measured by Plueddemann et al. (1998). The buoyancy frequency near 25-m depth is about 6 cycles per hour (cph). Assuming a near-inertial frequency of 1.05*f*, the mean vertical displacements associated with these waves are roughly 1 m, in agreement with values found using the ITP data.

Deeper, the time series measured by the temperature sensor chain is coherent in depth, consistent with low-mode vertical heaving of the water column (Timmermans et al. 2010). Converting the temperature anomalies to a vertical displacement by using the mean vertical gradients, the spectrum of vertical displacement shows high subinertial energy, and a well-defined inertial peak (Fig. A1b). The near-inertial peak in displacement is what the method outlined in the paper captures (in the upper ocean). The buoyancy frequency near 2600 m is about 0.25 cph. In both cases the energy level of the internal wave continuum (between *f* and *N*) is about one order of magnitude smaller than the Garrett–Munk spectral level, as observed previously (e.g., Levine et al. 1985, 1987). Note that the Garrett–Munk spectrum has no energy for displacements at the inertial frequency, but a large amount of near-inertial variance is observed in the deep ocean.

REFERENCES

Alford, M. H., 2003: Improved global maps and 54-year history of wind-work on ocean inertial motions. *Geophys. Res. Lett.,* **30,** 1424, doi:10.1029/2002GL016614.

Cavalieri, D., C. Parkinson, P. Gloersen, and H. J. Zwally, cited 2008: Sea ice concentrations from *Nimbus-7* SMMR and DMSP SSM/I passive microwave data. National Snow and Ice Data Center, Boulder, CO, digital media. [Available online at nsidc.org/data/nsidc-0051.html.]

D'Asaro, E. A., 1985: The energy flux from the wind to near-inertial motions in the surface mixed layer. *J. Phys. Oceanogr.,* **15,** 1043–1059.

——, and M. D. Morehead, 1991: Internal waves and velocity fine-structure in the Arctic Ocean. *J. Geophys. Res.,* **96** (C7), 12 725–12 738.

——, and J. H. Morison, 1992: Internal waves and mixing in the Arctic Ocean. *Deep-Sea Res. I,* **39** (Suppl.), S459–S484.

Emery, W. J., and E. T. Richard, 1998: *Data Analysis Methods in Physical Oceanography*. Elsevier Science and Technology, 654 pp.

Fer, I., R. Skogseth, and F. Geyer, 2010: Internal waves and mixing in the marginal ice zone near the Yermak Plateau. *J. Phys. Oceanogr.,* **40,** 1613–1630.

Garrett, C., 2001: What is the ''near-inertia'' band and why is it different from the rest of the internal wave spectrum? *J. Phys. Oceanogr.,* **31,** 962–971.

——, and W. Munk, 1972: Oceanic mixing by breaking internal waves. *Deep-Sea Res.,* **19,** 823–832.

Gimbert, F., D. Marsan, J. Weiss, N. C. Jourdain, and B. Barnier, 2012: Sea ice inertial oscillations in the arctic basin. *The Cryosphere,* **6,** 1187–1201.

Gregg, M. C., and E. Kunze, 1991: Shear and strain in Santa Monica Basin. *J. Geophys. Res.,* **96** (C9), 16 709–16 719.

Guthrie, J. D., J. H. Morison, and I. Fer, 2013: Revisiting internal waves and mixing in the Arctic Ocean. *J. Geophys. Res.,* **118,** 3966–3977, doi:10.1002/jgrc.20294.

Hakkinen, S., A. Proshutinsky, and I. Ashik, 2008: Sea ice drift in the Arctic since the 1950s. *Geophys. Res. Lett.,* **35,** L19704, doi:10.1029/2008GL034791.

Jackson, J. M., E. C. Carmack, F. A. McLaughlin, S. E. Allen, and R. G. Ingram, 2010: Identification, characterization, and change of the near-surface temperature maximum in the Canada Basin, 1993-2008. *J. Geophys. Res.,* **115,** C05021, doi:10.1029/2009JC005265.

Johnson, G. C., J. M. Toole, and N. G. Larson, 2007: Sensor corrections for Sea-Bird SBE-41CP and SBE-41 CTDs. *J. Atmos. Oceanic Technol.,* **24,** 1117–1130.

Johnson, H. L., and C. Garrett, 2004: Effects of noise on Thorpe scales and run lengths. *J. Phys. Oceanogr.,* **34,** 2359–2372.

Kalnay, E., and Coauthors, 1996: The NCEP/NCAR 40-Year Reanalysis Project. *Bull. Amer. Meteor. Soc.,* **77,** 437–471.

Kanamitsu, M., W. Ebisuzaki, J. Woollen, S. K. Yang, J. J. Hnilo, M. Fiorino, and G. L. Potter, 2002: NCEP-DOE AMIP-II Reanalysis (R-2). *Bull. Amer. Meteor. Soc.,* **83,** 1631–1643.

Kowalik, Z., and A. Y. Proshutinsky, 1994: The Arctic Ocean tides. *The Polar Oceans and Their Role in Shaping the Global Environment, Geophys. Monogr,* Vol. 85, 137–158.

Krishfield, R., J. Toole, A. Proshutinsky, and M. L. Timmermans, 2008: Automated ice-tethered profilers for sea water observations under pack ice in all seasons. *J. Atmos. Oceanic Technol.,* **25,** 2091–2105.

Leaman, K. D., and T. B. Sanford, 1975: Vertical energy propagation of inertial waves—Vector spectral analysis of velocity profiles. *J. Geophys. Res.,* **80,** 1975–1978.

Lenn, Y.-D., T. P. Rippeth, C. P. Old, S. Bacon, I. Polyakov, V. Ivanov, and J. Hoelemann, 2011: Intermittent intense turbulent mixing under ice in the Laptev Sea Continental Shelf. *J. Phys. Oceanogr.,* **41,** 531–547.

Levine, M. D., C. A. Paulson, and J. H. Morison, 1985: Internal waves in the Arctic Ocean—Comparison with lower-latitude observations. *J. Phys. Oceanogr.,* **15,** 800–809.

——, ——, and ——, 1987: Observations of internal gravity waves under the Arctic pack ice. *J. Geophys. Res.,* **92** (C1), 779–782.

McLaughlin, F. A., E. C. Carmack, W. J. Williams, S. Zimmermann, K. Shimada, and M. Itoh, 2009: Joint effects of boundary currents and thermohaline intrusions on the warming of Atlantic water in the Canada Basin, 1993–2007. *J. Geophys. Res.,* **114,** C00A12, doi:10.1029/2008JC005001.

Merrifield, M. A., and R. Pinkel, 1996: Inertial currents in the Beaufort Sea: Observations of response to wind and shear. *J. Geophys. Res.,* **101** (C3), 6577–6590.

Overland, J. E., 2009: Meteorology of the Beaufort Sea. *J. Geophys. Res.,* **114,** C00A07, doi:10.1029/2008JC004861.

Padman, L., and S. Erofeeva, 2004: A barotropic inverse tidal model for the Arctic Ocean. *Geophys. Res. Lett.,* **31,** L02303, doi:10.1029/2003GL019003.

Pedlosky, J., 2003: *Waves in the Ocean and Atmosphere: Introduction to Wave Dynamics.* Springer, 263 pp.

Pinkel, R., 2005: Near-inertial wave propagation in the western Arctic. *J. Phys. Oceanogr.,* **35,** 645–665.

Plueddemann, A. J., R. Krishfield, T. Takizawa, K. Hatakeyama, and S. Honjo, 1998: Upper-ocean velocities in the Beaufort gyre. *Geophys. Res. Lett.,* **25,** 183–186.

Proshutinsky, A., and Coauthors, 2009: Beaufort gyre freshwater reservoir: State and variability from observations. *J. Geophys. Res.,* **114,** C00A10, doi:10.1029/2008JC005104.

Rainville, L., and P. Winsor, 2008: Mixing across the Arctic Ocean: Microstructure observations during the Beringia 2005 expedition. *Geophys. Res. Lett.,* **35,** L06806, doi:10.1029/2008GL033532.

——, C. M. Lee, and R. A. Woodgate, 2011: Impact of wind-driven mixing in the Arctic Ocean. *Oceanography,* **24,** 136–145.

Serreze, M. C., M. M. Holland, and J. Stroeve, 2007: Perspectives on the Arctic's shrinking sea-ice cover. *Science,* **315,** 1533–1536.

Steele, M., W. Ermold, and J. Zhang, 2011: Modeling the formation and fate of the near-surface temperature maximum in the Canadian Basin of the Arctic Ocean. *J. Geophys. Res.,* **116,** C11015, doi:10.1029/2010JC006803.

Thorpe, S. A., 1977: Turbulence and mixing in a Scottish Loch. *Philos. Trans. Roy. Soc. London,* **A286,** 125–181, doi:10.1098/rsta.1977.0112.

Timmermans, M. L., J. Toole, R. Krishfield, and P. Winsor, 2008a: Ice-tethered profiler observations of the double-diffusive staircase in the Canada Basin thermocline. *J. Geophys. Res.,* **113,** C00A02, doi:10.1029/2008JC004829.

——, ——, A. Proshutinsky, R. Krishfield, and A. Plueddemann, 2008b: Eddies in the Canada Basin, Arctic Ocean, observed from ice-tethered profilers. *J. Phys. Oceanogr.,* **38,** 133–145.

——, L. Rainville, L. Thomas, and A. Proshutinsky, 2010: Moored observations of bottom-intensified motions in the deep Canada Basin, Arctic Ocean. *J. Mar. Res.,* **68** (3–4), 625–641, doi:10.1357/002224010794657137.

Toole, J. M., M. L. Timmermans, D. K. Perovich, R. A. Krishfield, A. Proshutinsky, and J. A. Richter-Menge, 2010: Influences of the ocean surface mixed layer and thermohaline stratification on Arctic Sea ice in the central Canada Basin. *J. Geophys. Res.,* **115,** C10018, doi:10.1029/2009JC005660.

——, R. A. Krishfield, M.-L. Timmermans, and A. Proshutinsky, 2011: The ice-tethered profiler: Argo of the Arctic. *Oceanography,* **24,** 126–135.

Walsh, D., and E. Carmack, 2003: The nested structure of Arctic thermohaline intrusions. *Ocean Modell.,* **5,** 267–289.